Word count: 9351

REVISION 1

Elastic anomalies across the $P2_1mn \rightarrow Pnnm$ structural phase transition in δ-(Al,Fe)OOH

Niccolò Satta[1,2,3,*], Giacomo Criniti[1,†], Alexander Kurnosov[1], Tiziana Boffa Ballaran[1], Takayuki Ishii[4] and Hauke Marquardt[2]

[1]Bayerisches Geoinstitut, University of Bayreuth, 95447 Bayreuth, Germany
[2]Department of Earth Sciences, University of Oxford, OX1 3AN Oxford, United Kingdom
[3]Institut für Mineralogie, Westfälische Wilhelms-Universität Münster, 48149 Münster, Germany
[4]Institute for Planetary Materials, Okayama University, Misasa, 682-0193 Tottori, Japan
[†]Present address: Earth and Planets Laboratory, Carnegie Institution for Science, 20015 Washington, DC, USA

*Corresponding author: Niccolò Satta (nsatta@uni-muenster.de)

Abstract

Hydrogen may be recycled into the Earth's lower mantle by subduction and stabilized in solid solutions between phase H ($MgSiO_4H_2$), δ-AlOOH, ε-FeOOH, and SiO_2 post-stishovite. In high-pressure oxyhydroxide phases, hydrogen is incorporated following the typical (OHO) sequence, adopting the asymmetric configuration O-H···O that evolves into a symmetric disordered state upon compression. Moreover these iron-/aluminum-bearing oxyhydroxides [δ-(Al,Fe)OOH] present a structural phase transition from $P2_1nm$ to $Pnnm$ as pressure increases. Here, the single-crystal elasticity of the $P2_1nm$ phase of δ-($Al_{0.97}$,$Fe_{0.03}$)OOH has been experimentally measured across the $P2_1nm \rightarrow Pnnm$ transition up to 7.94(2) GPa by simultaneous single-crystal X-ray diffraction (XRD) and Brillouin spectroscopy at high pressures. The transition appears to be continuous, and it can be described with a second, fourth and six order terms Landau potential. Our results reveal an enhanced unit-cell volume compressibility, which is linked to an increase of the *b*- and *a*-axes linear compressibility in the $P2_1nm$ phase of δ-($Al_{0.97}$,$Fe_{0.03}$)OOH prior to the transition. In addition, we observed the presence of elastic softening in the $P2_1nm$ phase that mostly impacts the elastic stiffness coefficients c_{12}, c_{22} and c_{23}. The observed elastic anomalies cause a significant change in the pressure dependence of the adiabatic bulk modulus (K_S). These results provide a better understanding of the relation between elasticity, $P2_1mn \rightarrow Pnnm$ structural phase transition and hydrogen dynamics in δ-($Al_{0.97}$,$Fe_{0.03}$)OOH, which may be applied to other O-H···O-bearing materials.

1. Introduction

Hydrogen can be stored in mantle minerals, affecting their physical properties. Investigating its distribution throughout the Earth's interior is thus relevant to understanding deep geodynamic processes and geochemical cycles (Bercovici & Karato, 2003; Ohtani et al., 2004;

Ohtani, 2020). In the Earth's interior, hydrogen is mostly present as hydroxyl groups (OH^-) bonded to the crystal structure of hydrous phases, as well as incorporated as hydrous defect in nominally anhydrous minerals (Ishii et al., 2022; Jacobsen, 2006; Ohtani, 2015).

Solid solutions between isostructural compounds phase H ($MgSiO_4H_2$), δ-AlOOH, ε-FeOOH, and SiO_2 post-stishovite may act as main carriers of hydrogen into the lower mantle due to their ability to remain stable at relatively high-temperatures and pressures (Ishii et al., 2022; Nishi et al., 2019; Ohira et al., 2014). In iron-bearing aluminum oxyhydroxides [δ-(Al,Fe)OOH], hydrogen is expected to be bonded via hydrogen bonds adopting an asymmetrical configuration (O-H···O) at low pressures (Sano-Furukawa et al., 2018). Upon compression, symmetrization of the hydrogen bonds (O-H-O) is achieved with a symmetric proton disordered state acting as a precursor to the symmetrization (Sano-Furukawa et al., 2018). The phenomenon of hydrogen bond symmetrization is predicted to impact physical properties, potentially enhancing the stability of these oxyhydroxides down to the core-mantle boundary (Nishi et al., 2019; Ohira et al., 2014).

At ambient conditions, the crystal structure of δ-AlOOH and ε-FeOOH (Supplementary Figure S1a) has space group $P2_1nm$ and consists of chains of edge sharing $(Al,Fe)O_6$ octahedra extending parallel to the **c**-axis and connected with each other through vertices (Bolotina et al., 2008; Komatsu et al., 2006; Kuribayashi et al., 2014; Pernet et al., 1975; Suzuki et al., 2000; Suzuki, 2010). The octahedral cation site is coordinated by three oxygen atoms and three hydroxide, which gives rise to a 2D hydrogen bond network in the **a-b** plane, with the hydrogen bonds lying almost parallel to the [120] direction (Kuribayashi et al., 2014; Sano-Furukawa et al., 2018). Below 10 GPa, a structural phase transition occurs in δ-AlOOH, resulting in the symmetry increasing from $P2_1nm$ to $Pnnm$ (Supplementary Figure S1b) (Kuribayashi et al., 2014; Sano-Furukawa et al., 2009; Simonova et al., 2020). Within the same pressure range, neutron diffraction experiments by Sano-Furukawa et al. (2018) showed a change in the hydrogen bond from an asymmetric ordered configuration (O-H···O) to a symmetric disordered one where hydrogen atoms are equally distributed between two symmetrically-equivalent sites across the center of the O···O line (Supplementary Figure S1b). The disordering of hydrogen in the 9-18 GPa range has been initially attributed to the presence of proton tunneling, similarly to previous observations in high-pressure H_2O ices (Lin et al., 2011; Meier et al., 2018; Trybel et al., 2020), whereas more recent studies suggested that it is actually dynamic disorder (Meier et al., 2022; Trybel et al., 2021). Centering of the hydrogen bond, i.e. with the hydrogen locked in the mean position along the O···O line and covalently bonded to the two oxygens (O-H-O), occurs in δ-AlOOH at around 16-18 GPa (Sano-Furukawa et al., 2018), or possibly at even lower pressures (14.7 GPa, Trybel et al., 2021). Therefore, proton disordering appears to act as precursor to the hydrogen bond symmetric centered configuration.

Theoretical studies suggest that the completion of the symmetrization of the hydrogen bonds would severely alter the elastic properties of δ-AlOOH (Cortona, 2017; Panero & Stixrude, 2004; Pillai et al., 2018; Tsuchiya et al., 2002; Tsuchiya & Tsuchiya, 2009). Experimental observations of this occurrence were provided by Brillouin scattering measurements on polycrystalline samples of δ-AlOOH (Mashino et al., 2016) and δ-$(Al_{0.95}Fe_{0.05})OOH$ (Su et al., 2020) that detected a sharp change in acoustic wave velocities at ~15 and ~20 GPa, respectively. However, previous *P-V* experimental investigations on δ-(Al,Fe)OOH contrast with this interpretation since a reduction in the axial compressibility was observed at much lower pressures (~ 8 GPa; e.g., Ohira et al., 2019; Sano-Furukawa et al., 2009), hence suggesting that it is the $P2_1nm \rightarrow Pnnm$ transition that mostly impacts the compression behavior of these oxyhydroxides.

At the Fe-rich end of the solid solution series, recent experimental studies pinpointed the $P2_1nm \rightarrow Pnnm$ transition in δ-($Al_{0.3}Fe_{0.7}$)OOH and ε-FeOOH at ~10 GPa and 18 GPa, respectively (Ikeda et al., 2019; Meier et al., 2021; Thompson et al., 2017, 2020). Additionally, a high-to-low spin transition in Fe has been found to occur in ε-FeOOH at about 45 GPa (Gleason et al., 2013; Thompson et al., 2020), but the symmetrization pressure in ε-FeOOH is still poorly constrained. This has been first suggested to occur around 45 GPa, and linked to the Fe spin transition (Gleason et al., 2013; Xu et al., 2013). However, more recent experimental studies on δ-($Al_{0.3}Fe_{0.7}$)OOH showed that these are two distinct phenomena (Meier et al., 2022). Other studies suggest the symmetrization to occur at lower pressures, between 10 and 20 GPa, and possibly triggering the $P2_1nm \rightarrow Pnnm$ transition in ε-FeOOH (Thompson et al., 2017).

Therefore, in spite of the number of recent studies (e.g., Buchen et al., 2021; Insixiengmay & Stixrude, 2023; Luo et al., 2022; Mashino et al., 2016; Meier et al., 2022; Sano-Furukawa et al., 2018; Satta et al., 2021; Strozewski et al., 2023; Thompson et al., 2020; Trybel et al., 2021; Tsuchiya et al., 2020), the relation between elastic behavior, hydrogen bond disorder/symmetrization, and structural phase transition in δ-(Al,Fe)OOH is still poorly constrained, hampering our understanding of the deep recycling of hydrogen into the Earth's lower mantle.

Here, we performed simultaneous high-pressure X-ray diffraction (XRD) and Brillouin spectroscopy experiments on δ-($Al_{0.97}$,$Fe_{0.03}$)OOH samples to provide the first full and comprehensive description of the single-crystal elasticity of the $P2_1nm$ phase of δ-(Al,Fe)OOH at high pressure. Our experiments were performed up to 7.94(2) GPa with relatively small pressure steps across the $P2_1nm \rightarrow Pnnm$ transition in order to better constrain any small elastic change associated with the transition. Our results, that include the description of all the elastic stiffness coefficients at high pressures, provide new insights on the relation between single-crystal elasticity at high pressures, structural transition and proton disordering in δ-($Al_{0.97}$,$Fe_{0.03}$)OOH.

2. Materials and Methods

2.1. Samples

In this study, the same two single-crystal platelets of δ-($Al_{0.97}$,$Fe_{0.03}$)OOH studied at pressures above 8 GPa by Satta et al. (2021), namely H4765x1 and H4765x2, were measured. Details on the synthesis procedure, chemical compositions of each crystal platelet, as well as sample selection, orientation and preparation, can be found in Satta et al. (2021).

2.2. High-Pressure Experiments

High-pressure experiments were performed using a BX90 diamond anvil cell (DAC) (Kantor et al., 2012) equipped with Boehler-Almax type diamonds (Boehler & De Hantsetters, 2004) having a culet size of 400 μm. A circular pressure chamber (250 μm diameter) was obtained by laser drilling a Re gasket previously indented to a final thickness of about 50 μm. Both sample platelets were loaded in the pressure chamber (Schulze et al., 2017), together with a ruby ($Cr:Al_2O_3$) sphere for pressure determination. Ruby fluorescence measurements on the pressurized ruby and on a ruby sphere kept at room pressure were performed before and after each set of experiments. Room pressure and pressurized rubies were kept at the same temperature for at least 4 hours before the fluorescence measurements. The ruby calibration of Dewaele et al. (2004) was used to derive pressures from the ruby fluorescence signal.

High-pressure experiments were performed in two distinct runs, with He or Ne acting as pressure-transmitting media (Supplementary Table S1). Both Ne and He ensure a quasi-hydrostatic environment within the investigated pressure range (Klotz et al., 2009). Gas loadings were performed using the system installed at the BGI (Kurnosov et al., 2008). Simultaneous single-crystal XRD and Brillouin spectroscopy experiments at high pressure were conducted up to 7.94(2) GPa using the combined XRD and Brillouin spectroscopy system installed at the BGI (Trots et al., 2011, 2013).

The unit-cell parameters and volumes of the two single-crystal platelets (Table S1) were determined for each platelet by centering a minimum of 12, and up to 17 Bragg reflections (21° < 2θ < 40°) belonging to the <111>, <120>, <021>, <211>, <121>, <030>, <301>, <112>, <031>, <131>, <202>, <212>, <411> and <222> families of crystallographic planes. The centering routine employed in our study relies on the eight position protocol described by King & Finger (1979) to correct for diffractometer aberrations and sample offsets using a Huber four-circle diffractometer. The diffractometer is equipped with an ultra-high intensity Mo$K\alpha$ rotating anode X-ray source (FR-E+ SuperBright, Rigaku) coupled with multilayer VaryMax™ focusing optics and a point detector, and is operated using the SINGLE software (Angel & Finger, 2011). Due to the non-homogeneous $K\alpha_1/K\alpha_2$ ratio produced by the X-ray focusing optics, individual reflection profiles were refitted using the WinIntegrStp software (Angel, 2003). The unit-cell parameters of the two crystals (Table S1) are not identical due to their slightly different Fe contents, that is 3.24(15) wt% for H4765x1 and 2.71(15) wt% for H4765x2 (Satta et al. 2021). Note, however, that such subtle difference in Fe content has a negligible effect on both the compressibility and elasticity behavior of the two crystals (see Results and Discussion below).

Brillouin spectroscopy experiments were performed in a 80° forward symmetric scattering geometry (Speziale et al., 2014; Whitfield et al., 1976) using a coherent Verdi V2 solid state Nd:YVO_4 frequency doubled laser (λ_0 = 532.0 nm), and a six-pass scanning Fabry-Pérot interferometer (Lindsay et al., 1981; Sandercock, 1982) coupled to a single pixel photon counter detector. Measurements were performed at a total of nine distinct pressure points, from room pressure to 7.94(2) GPa. Brillouin spectra were collected for each pressure point and for each platelet at different rotation angles (χ) with 10-20° interval over a 360° angular range. The external scattering angle (Θext) was calibrated with a reference silica glass. Frequency shifts were converted into velocities using the equation (Speziale et al., 2014; Whitfield et al., 1976):

$$v = \frac{\Delta\omega\ \lambda_0}{2\sin\left(\frac{\Theta ext}{2}\right)} \quad (1)$$

Where $\Delta\omega$ is the measured frequency shift, λ_0 is the laser wavelength in air (and vacuum) and $\Theta ext = 80^\circ$. The $P2_1nm$ phase of δ-(Al,Fe)OOH crystalizes in the orthorhombic system, hence its single-crystal elasticity is described by nine independent, non-zero elastic stiffness coefficients (c_{ij}). In Voigt notation (Nye, 1985), these are: c_{11}, c_{22}, c_{33}, c_{44}, c_{55}, c_{66}, c_{12}, c_{13}, c_{23}. All nine c_{ij} were constrained at each pressure point (Table S3) through a least-square fit of the Christoffel equation (Haussühl, 2007):

$$\left|c_{ijkl}n_j n_l - \rho v^2 \delta_{ik}\right| = 0 \quad (2)$$

where c_{ijkl} are the elastic stiffness coefficients in full tensorial notation, n_j and n_l are the phonon direction cosines, ρ is the density and δ_{ik} is the Kronecker delta. The least-square fitting routine of the Christoffel equation was implemented in an Origin software (OriginLab corporation, Northampton, MA, USA) script following the formulation by Buchen (2018). The densities of the two platelets were calculated taking into account the different compositions of the two crystals (Table S1) as well as the fact that the synthesis was performed using a 96% ^{57}Fe enriched starting material (Satta et al. 2021). The two densities were found to be identical within uncertainties, hence an averaged value (Table S3) was used in the fitting routine. Voigt and Reuss bounds of the adiabatic bulk (K_S) and shear moduli (G) were calculated at each pressure point using the c_{ij} and the elastic compliance coefficients, s_{ij}, respectively (Table S4).

3. Results and Discussion

3.1. $P2_1nm \rightarrow Pnnm$ transition pressure

The evolution of the $0\bar{3}0$ reflection of sample H4765x2 was followed as a function of pressure in order to pinpoint the $P2_1nm \rightarrow Pnnm$ transition pressure (Figure 1). This reflection is intense in the $P2_1nm$ space group and is a systematic extinction in the $Pnnm$ space group in which only the *0k0*, with *k=2n* reflections can be observed. The intensity of the $0\bar{3}0$ reflection has been normalised with respect to that of the $1\bar{3}0$ reflection, which is present in both $P2_1nm$ and $Pnnm$ space groups. For this purpose, the omega rocking curves (inset in Figure 1) for the two reflections were measured at each pressure using omega steps of 0.005° and exposure times up to 10 s/step. The crystalline quality of both platelets, assessed from the full width half maximum of investigated reflection peaks in omega rocking curves, was found to be preserved after the phase transition. Our results show that the intensity ratio $I(0\bar{3}0)/I(1\bar{3}0)$ decreases continuously and non-linearly with pressure, eventually reaching zero with the disappearance of the $0\bar{3}0$ reflection between P_{ruby} 7.59(3) GPa and 7.94(2) GPa. If we assume that this intensity ratio varies as the square of the order parameter, Q, driving the $P2_1nm \rightarrow Pnnm$ phase transition, then a Landau free energy (G) expansion having second, fourth and sixth order terms $G = \frac{1}{2}a(P - P_c)Q^2 + \frac{1}{4}bQ^4 + \frac{1}{6}cQ^6$ (e.g., Carpenter et al., 1998) can be used to derive the variation of Q^2 with pressure (Boffa Ballaran et al., 2000; Carpenter et al., 1990):

$$Q^2 = \frac{I(0\bar{3}0)}{I(1\bar{3}0)} = \frac{1}{2}\frac{-\frac{b}{a} + \sqrt{\left(\frac{b}{a}\right)^2 - 4\frac{c}{a}(P - Pc)}}{\frac{c}{a}} \tag{3}$$

With P_c being the transition pressure, and *a, b* and *c* the Landau coefficients. Note that only relative values of the coefficients have been used since the absolute values of *a*, *b* and *c* cannot be constrained without additional information (e.g. excess heat capacity). Fit to the intensity ratio data (Figure 1) gives P_c =7.7(2) GPa, and the ratio between the coefficients (in GPa) are 10(5) and 56(19) for *b/a* and *c/a,* respectively.

The disappearance of the 010 and 120 reflections of the δ-AlOOH end-member has been previously observed to occur at lower pressures (i.e. at 4.83 GPa and at 6.53 GPa, respectively) in neutron diffraction experiments (Sano-Furukawa et al., 2009). On the other hand, single-crystal X-ray diffraction experiments on the same end-member δ-AlOOH, reported the disappearance of selected *0kl* reflections with $k + l$ = odd (i.e. systematic extinction in the *Pnnm* space group) between 6.1 and 8.2 GPa (Kuribayashi et al., 2014), hence in excellent agreement with our results. The disappearance of the $0\bar{3}0$ reflection is associated with a change in the pressure dependence of the unit-cell axial ratios *a*/*b*, *b*/*c* and *a*/*c* (Supplementary Figure S2), which becomes particularly evident when our data are plotted together with those of the *Pnnm* phase of δ-$(Al_{0.97},Fe_{0.03})OOH$ from Satta et al. (2021). A similar behavior in axial ratios was previously observed within the same pressure range in δ-AlOOH (Kuribayashi et al., 2014; Sano-Furukawa et al., 2009), $(Al_{0.832}Fe_{0.117})OOH_{1.15}$ and $(Al_{0.908}Fe_{0.045})OOH_{1.14}$ (Ohira et al., 2019), suggesting that the incorporation of about 3% of Fe^{3+} into the δ-AlOOH structure has a negligible effect on the $P2_1nm \rightarrow Pnnm$ transition pressure. Note that larger Fe contents, however, are expected to increase the transition pressure, since the $P2_1nm \rightarrow Pnnm$ phase transition in the end-member ε-FeOOH was observed at 18 GPa (Thompson et al., 2020).

Typically, a substituting atom in a solid solution only affects the transition point of the end-member once the microscopic strain fields created by the individual substitutions start to overlap.

As Fe^{3+} atoms are added into the δ-AlOOH structure, we would expect the $P2_1nm \rightarrow Pnnm$ transition pressure to remain constant below a critical composition, which is a direct reflection of the magnitude of the strain fields created by the cation substitution (e.g., Boffa Ballaran et al., 2000; Carpenter et al., 1999; Carpenter et al., 2009; Hayward & Salje, 1996). As there are two cation sites in the unit-cell, the richest Fe-bearing δ-AlOOH studied by Ohira et al. (2019) (i.e., sample Fe12) consist of ~ one atom of Fe^{3+} for every 4 unit-cells. Since no effect on the transition pressure has been observed also for our samples, we expect that a larger concentration of Fe is necessary to observe any change in the behavior of the $P2_1nm \rightarrow Pnnm$ transition as a result of the Al-Fe cation substitution.

3.2. Compression behavior

The unit-cell volumes of H4765x1 and H4765x2 are listed in Supplementary Table S1, and their variations with pressure are reported in Figure 2a. The two platelets show the same compressional behavior up to the last pressure point measured. Only unit-cell volumes observed at $P_{\text{ruby}} \leq 6.46(2)$ GPa have been fitted using a 3rd-order Birch-Murnaghan equation of state (BM3) (Birch, 1947) implemented in the EoSFit7 software (Angel et al., 2014) to give insight on possible volume anomalies associated with the $P2_1nm \rightarrow Pnnm$ transition. The volume at room pressure, V_0, as well as the isothermal bulk modulus, K_{T0}, and its pressure derivative, K'_{T0}, were fitted using data weighted by the uncertainties in both P and V. The resulting BM3 parameters are reported in Supplementary Table S2.

The value of 150.6(11) GPa for K_{T0} obtained in this study is in good agreement with previous experimental studies on the $P2_1nm$ phase of δ-AlOOH and δ-(Al,Fe)OOH (Ohira et al., 2019; Sano-Furukawa et al., 2009) which, however, have used a 2nd-order Birch-Murnaghan for fitting the *P-V* data. Our results, instead, tightly constrain the K'_{T0} of the $P2_1nm$ phase of δ-($Al_{0.97}Fe_{0.03}$)OOH, which appears to be slightly smaller than 4 (Supplementary Table S2). Additionally, it is possible to observe a subtle deviation of the volume data from the BM3 EoS fit at $P_{ruby} > 6.46(2)$ GPa (Figure 2a and inset). Specifically, the observed volumes are smaller than those predicted by the BM3, suggesting a softening of K_T prior to the $P2_1nm \rightarrow Pnnm$ transition. Similar observations have been reported for high-pressure H_2O ices (e.g. Méndez et al., 2021; Shi et al., 2021; Sugimura et al., 2008) and other mineral phase transformations (e.g. Arlt & Angel, 2000; Carpenter et al., 2003; Carpenter & Zhang, 2011; McConnell et al., 2000).

The linear moduli, *k*, and their first pressure derivatives, *k*′, have been obtained by fitting our observed unit-cell parameters at $P_{ruby} \leq 6.46(2)$ (Supplementary Table S1) with linearized BM3 implemented in EosFit7 (Angel et al., 2014). Fit results are listed in Supplementary Table S2. The unit-cell *a* and *b* parameters measured at $P_{ruby} > 6.46(2)$ deviate from the BM3 fit, whereas the *c*-axis does not exhibit any anomalous behavior in the investigated pressure range (Figure 2b).

The axial compressibility of the $P2_1nm$ phase follows the scheme $\beta_b > \beta_a > \beta_c$ (Figure 2b), in agreement with previous reports (Ohira et al., 2019; Sano-Furukawa et al., 2009). This compressibility scheme is due to the different axial response of the δ-($Al_{0.97}Fe_{0.03}$)OOH structure to compression, with the **a-b** plane being relatively compressible due to the presence of hydrogen bonds in the asymmetric configuration (Supplementary Figure S1a), whereas chains of edge-sharing octahedra extend along the *c*-axis giving rise to a stiffer unit to be compressed. With increasing pressure, however, the compressibility of the *a*-axis (and to smaller extent that of the *b*-axis) decreases quickly as indicated by their relatively large moduli pressure derivatives, which may be due to the shortening of the O···O distance and a consequent increase of the strengths of the hydrogen bonds, as already suggested by previous studies on δ-AlOOD (Sano-Furukawa et al., 2008). After the transition to the high-symmetry phase, a stiffening of the *a*- and *b*- axes in δ-($Al_{0.97}Fe_{0.03}$)OOH have been previously observed, with the axial compressibilities evolving into a $\beta_c > \beta_a > \beta_b$ scheme (Satta et al., 2021). Thus, our results confirm that the phase transition in δ-($Al_{0.97}Fe_{0.03}$)OOH induces a marked stiffening of the **a-b** plane, supporting previous findings (Ohira et al., 2019; Sano-Furukawa et al., 2009).

3.3. Single-crystal elasticity

A representative Brillouin spectrum collected for crystal H4765x2 at high pressures is shown in Figure 3a, while measured and calculated acoustic velocities obtained for both platelets at the same pressure are shown in Figure 3b. Full elastic stiffness tensors of δ-($Al_{0.97}$,$Fe_{0.03}$)OOH constrained at nine different pressure points are reported in Supplementary Table S3, and individual elastic stiffness coefficients are plotted against pressure in Figure 4.

The $P2_1nm$ is a polar space group (i.e. it is not centrosymmetric). Thus, piezoelectricity may exert an influence on acoustic waves velocities propagating in the $P2_1nm$ phase of δ-(Al,Fe)OOH along specific directions (Every, 1980; Nye, 1985). Here, possible contributions to the acoustic wave velocities from the piezoelectricity were neglected, as in previous Brillouin spectroscopy experiments on δ-AlOOH (Wang et al., 2022). We find this to be a reasonable assumption given the good agreement between our K_{T0} resulting from X-ray diffraction experiments (hence not sensitive to piezoelectricity), and K_{S0} resulting from c_{ij} determined via inversion of observed acoustic wave velocities in a least square fitting of the Christoffel equation. Note also that for those materials for which the piezoelectric tensor has been determined at room pressure, e.g., quartz (Ohno, 1990) and $Ca_3TaGa_3Si_2O_{14}$ (Ma et al., 2017), a correction of c_{ij}

accounting for piezoelectric contribution is <1%, hence further suggesting that the piezoelectric contribution to acoustic wave velocity can be reasonably neglected in our study.

The elastic stiffness tensor obtained at room pressure in this study shows a good agreement with the theoretical predictions reported by Cortona (2017), with the exception of c_{22} which is about 20% higher than that determined in this study (Figure 4). Tsuchiya & Tsuchiya (2009) generally report smaller c_{ij} values than those constrained in this study; c_{11}, for example, is about 20% smaller. On the other hand, Pillai et al. (2018) report generally larger c_{ij} values compared to those measured here (up to 30%). Our results are also in good agreement with previous Brillouin spectroscopy measurements performed at room pressure on the $P2_1nm$ phase of pure δ-AlOOH (Wang et al., 2022) (Figure 4).

We found that the pressure dependence of all c_{ij} determined in this study up to P_{ruby} = 6.46(2) GPa can be described by a third-order finite strain expression reported for individual c_{ijkl} by Stixrude & Lithgow-Bertelloni (2005):

$$\begin{aligned} c_{\mathrm{ijkl}} = (1+2f)^{\frac{5}{2}} \{ & c_{\mathrm{ijkl},0} + \left(3K_0 c'_{\mathrm{ijkl},0} - 5c_{\mathrm{ijkl},0}\right)f + \\ & + \left[6K_0 c'_{\mathrm{ijkl},0} - 14c_{\mathrm{ijkl},0} - \frac{3}{2}K_0 \delta^{\mathrm{ij}}_{\mathrm{kl}}(3K'_0 - 16)\right] f^2 \} \end{aligned} \tag{4}$$

with the Eulerian strain $f = \left[\left(\frac{V}{V_0}\right)^{-2/3} - 1\right]/2 = \left[\left(\frac{\rho}{\rho_0}\right)^{2/3} - 1\right]/2$, with $c_{\mathrm{ijkl},0}$ and $c'_{\mathrm{ijkl},0}$ being the elastic stiffness coefficients and their pressure derivative at room pressure expressed in full tensorial notation, respectively and with δ^{ij}_{kl} being -3 for c_{1111}, c_{2222} and c_{3333} and -1 for the other six independent coefficients of the elastic tensor.

At high pressures, our results are generally in good agreement with previous theoretical predictions at 5 GPa for the $P2_1nm$ phase of δ-AlOOH (Cortona, 2017), except for c_{22} and the off-diagonal c_{ij}. Additionally, our results clearly show an elastic softening at P_{ruby} > 6.46(2) GPa affecting c_{12}, c_{22} and c_{23}. This observation corroborates the presence of an elastic softening observed by our XRD experiments on the axial and volume compression within the same pressure range (Figure 2). The transition to the high-symmetry phase gives rise to an abrupt step increase (~ 50%) of c_{12}, c_{22} and c_{23}, while all the other c_{ij} show relatively low sensitivity to the phase transition. In general, theoretical studies suggest that the hydrogen bond symmetrization has a severe influence on the elastic behavior of δ-AlOOH. This has been either expressed by a smooth stiffening of the compressional and off-diagonal c_{ij} (Cortona, 2017; Tsuchiya & Tsuchiya, 2009), or by a more complex behavior that may include softening and/or hardening within a relatively short symmetrization pressure range (11-16 GPa) (Pillai et al., 2018). Conversely, our results clearly show that important modifications in the single-crystal elasticity of δ-$(Al_{0.97},Fe_{0.03})OOH$ occur at much lower pressures than previously predicted, and are associated with the structural phase transformation. Additionally, we observed that shear c_{44}, c_{55} and c_{66} only show a limited sensitivity to the transition, in agreement with previous theoretical studies (Cortona, 2017; Pillai et al., 2018; Tsuchiya & Tsuchiya, 2009). Ultimately, it is possible that elastic softening of c_{12}, c_{22} and c_{23} observed in this study may couple with the softening of the O-H stretching optical modes observed in the $P2_1nm$ phase in previous Raman spectroscopy investigations (Wang et al., 2022).

3.4. Landau model

As observed above, a 2-4-6 Landau potential well describes the variation with pressure of the order parameter associated with the $P2_1nm \rightarrow Pnnm$ transition in δ-$(Al_{0.97},Fe_{0.03})OOH$. The same Landau potential can also be used to describe the evolution of the spontaneous strains associated with a displacive phase transition (Carpenter and Salje, 1998), with the Landau expansion being:

$$G = \frac{1}{2}a(P - P_c)Q^2 + \frac{1}{4}bQ^4 + \frac{1}{6}cQ^6 + \lambda_1 e_1 Q^2 + \lambda_2 e_2 Q^2 + \lambda_3 e_3 Q^2 + \frac{1}{2}\sum_{i,j} c_{ij}^0 e_i e_j \quad (5)$$

We note that Equation 5 is identical to that provided by Carpenter et al. (2003) for the *Pmcn* to *P*2₁*cn* phase transition occurring in lawsonite, but for pressure replacing temperature dependency. In Equation 5, λ_{1-3} are the coupling coefficients between the components of the spontaneous strains and the order parameter Q, e_{1-3} are the spontaneous strain components, and c_{ij}^0 are the "bare", i.e. not including the effect of the phase transition, elastic stiffness coefficients.

In our analysis, the evolution of c_{ij}^0 in the $P2_1nm$ stability field is obtained using self-consistent finite strain equations (Equation 4), following the approach delineated by previous studies (e.g. Buchen et al., 2018; Zhang et al., 2021). The extrapolation of c_{ij}^0 to experimental pressures relies on the room pressure elastic stiffness coefficients and respective pressure derivatives constrained for the *Pnnm* phase of δ-($Al_{0.97}$,$Fe_{0.03}$)OOH by Satta et al. (2021). Spontaneous strain components are defined as (Carpenter et al. 1998):

$$e_1 = \frac{a_L - a_H}{a_H}; \qquad e_2 = \frac{b_L - b_H}{b_H}; \qquad e_3 = \frac{c_L - c_H}{c_H} \quad (6)$$

Where the unit-cell axial lengths (a_L, b_L and c_L) of the $P2_1nm$ phase were determined via XRD in this study, and the values of the *Pnnm* phase (a_H, b_H and c_H) at $P < P_c$ were determined using linearized BM3 and the parameters given in Satta et al. (2021).

Ultimately, the coupling coefficients λ_{1-3} were constrained in a least-square fitting procedure of spontaneous strain expressions obtained from the Landau expansion under equilibrium conditions (Equations 2-4 in Carpenter et al. 2003). We find the Landau model to provide an excellent description of spontaneous strain components as a function of unit-cell volume compression (Supplementary Figure S3).

The variation of individual c_{ij} due to a structural phase transition (Carpenter and Salje 1998) can be defined using the relationship (Slonczewski and Thomas 1970):

$$c_{ij} = c_{ij}^{0} - \sum_{m,n} \frac{\partial^2 G}{\partial e_i \partial Q_m} \left(\frac{\partial^2 G}{\partial Q_m \partial Q_n} \right)^{-1} \frac{\partial^2 G}{\partial e_j \partial Q_n} \tag{7}$$

and considering that for the $P2_1nm \rightarrow Pnnm$ transition only one order parameter Q is active. The relationships between c_{ij}^{0} and Q are identical to those previously reported for lawsonite (Equations 17-25 in Carpenter et al., 2003). Accordingly, the susceptibility, χ, is defined as:

$$\chi^{-1} = \frac{\partial^2 G}{\partial Q^2} = a(P - P_c) + \frac{3b}{a} a Q^2 + \frac{5c}{a} a Q^4 + 2\lambda_1 e_1 + 2\lambda_2 e_2 + 2\lambda_3 e_3 \tag{8}$$

which can be seen an adaptation to the expression reported by Carpenter et al. (2003). This adaptation was employed to take into account constraints on b/a and c/a, as well as values the coupling coefficients λ_{1-3}. Here, these parameters were determined in a least-square fitting of Q^2 to the intensity ratio $I(0\bar{3}0)/I(1\bar{3}0)$, as previously described in Section 3.1, hence making a the only refined parameter in Equation 8 for c_{11}, c_{22}, c_{33}, c_{12}, c_{13} and c_{23}. As for the coupling coefficient λ_{4-6}, these have been determined by fitting measured c_{44}, c_{55} and c_{66} with appropriate expressions derived from Equation 7, and using the order parameter formulation described above (Equation 3).

We found the Landau-based predictions on the high-pressure behavior of c_{ij} to be only in partial agreement to those observed experimentally (Figure 4). Specifically, we note an excellent agreement between observations and Landau-based predictions for the shear c_{44}, c_{55} and c_{66} including a hardening prior to the $P2_1nm \rightarrow Pnnm$ transition. Also, there is a good agreement between observed and predicted c_{33} values, with the only difference being the Landau model predicting a subtle softening prior to the onset of the $P2_1nm \rightarrow Pnnm$ transition and in the $P2_1nm$ stability field which was, however, not observed experimentally. On the other hand, only a poor agreement is reached for all other c_{ij}, with experiments and theory agreeing solely on the presence of a softening affecting the c_{12}, c_{22} and c_{23} prior to the onset of the $P2_1nm \rightarrow Pnnm$ transition. Ultimately, the Landau-based model also predicts a softening of the c_{11} and c_{13}, hence contrasting with our experimental observations. Such discrepancies between Landau-based model and experimental observations may suggest that the order parameter associated with the displacive processes is not able to entirely describe the structural changes occurring in δ-($Al_{0.97}$,$Fe_{0.03}$)OOH. Therefore, taking into consideration higher order terms of the coupling between order parameter and spontaneous strain, and/or coupling coefficients dependent on pressure, may be necessary to obtain a better match between Landau prediction and experimental observations. At the same time, it is also possible that differences in relaxation times between proton ordering/disordering and displacive order parameter may play a role in the $P2_1nm \rightarrow Pnnm$ phase transition.

3.5. Aggregate properties

All our results on the aggregate properties of δ-($Al_{0.97}$,$Fe_{0.03}$)OOH are provided in Supplementary Table S4. The adiabatic bulk, K_S, and shear, G, moduli determined in this study at room pressure match previous experimental estimates for δ-AlOOH (Wang, et al., 2022), and are in good agreement with most previous theoretical results (Cortona, 2017; Tsuchiya & Tsuchiya, 2009). The K_S and G values are shown in Figure 5a as function of pressure. Our results show a marked softening of K_S above 6.46(2) prior to the onset of the $P2_1nm \rightarrow Pnnm$ phase transition, followed by a ~30% increase after the transition to the high-symmetry phase is completed. This elastic softening in K_S is linked to the softening of c_{12}, c_{22} and c_{23} observed in our single-crystal elasticity study. On the other hand, G increases smoothly with pressure and no marked stiffening is observed after the phase transition. The Reuss bound of the adiabatic bulk modulus (K_S^R, Table 1) and its pressure derivative are in good agreement with our XRD results. Our results confirm that Al-Fe^{3+} substitution may decrease both K_S and G since values reported for ε-FeOOH are sensibly smaller [K_S = 133(7) GPa and G = 71(2) GPa, Ikeda et al., 2019].

The calculated aggregate compressional, v_P $(=\sqrt{\frac{K_S^H + 4/3G^H}{\rho}})$ and shear, v_S $(=\sqrt{\frac{G^H}{\rho}})$, wave velocities are listed in Supplementary Table 4. The room pressure v_P and v_S values constrained in this study are in perfect agreement with previous Brillouin spectroscopy results on δ-AlOOH single-crystal elasticity (Wang et al., 2022). At the same time, v_P and v_S determined in this study are respectively about 4% and 7% higher than those observed in polycrystalline δ-AlOOH (Mashino et al., 2016), and about 4% and 10% than those on polycrystalline δ-$(Al_{0.95}Fe_{0.05})OOH$ (Su et al., 2020). These discrepancies between single-crystal and polycrystalline data cannot be ascribed to different Fe content, as Fe substituting Al decreases acoustic wave velocities (Ikeda et al., 2019), but may be related to the presence of lattice preferred orientation in the polycrystalline samples, selective elasto-optic coupling along specific directions (Speziale et al., 2014), the contribution of grain boundaries (Marquardt et al., 2011), or grain-grain-interactions (Wang et al., 2023). The pressure dependencies of both aggregate wave velocities are shown in Figure 5b. As v_P is proportional to the bulk modulus, it is possible to observe a slight softening above 6.46(2) GPa and a jump after the $P2_1nm$ to $Pnnm$ phase transition, whereas v_S show a smooth increase with pressure.

4. Implications

In this study, we provided accurate experimental constraints on the high-pressure, single-crystal elasticity of the $P2_1nm$ phase of δ-$(Al_{0.97},Fe_{0.03})OOH$ and characterised the $P2_1nm \rightarrow Pnnm$ phase transition occurring between P_{ruby} 7.59(3) GPa and 7.94(2) GPa. A 2-4-6 Landau potential has been used to describe the variation with pressure of the $I(0\bar{3}0)/I(1\bar{3}0)$ ratio constraining the transition pressure to be $P_c = 7.7(2)$ GPa.

Both XRD and Brillouin scattering results show elastic softening occurring in the $P2_1nm$ phase prior to the onset of the structural transition. The compressibility of the *b*- and *a*-axes increase from 6.46(2) GPa, up to the transition to the *Pnnm* phase, and is accompanied by a marked softening of the elastic stiffness coefficients c_{12}, c_{22} and c_{23}. These experimental findings were compared to those predicted by a 2-4-6 Landau model which show that the transition has a substantial displacive component with the order parameter and the spontaneous strain having a relaxation time on the order of that probed by the X-ray measurements. However, the Landau model does not reproduce the high-pressure evolution of most of the c_{ij} affected by transition, suggesting that proton order/disorder contributions to the transition may need to be taken into account to describe the elastic behavior of the $P2_1nm$ δ-($Al_{0.97}$,$Fe_{0.03}$)OOH.

The incorporation of the FeOOH component in δ-(Al,Fe)OOH shifts the structural transition toward transition zone pressures (Thompson et al., 2020). If the boundary between the $P2_1nm$ and *Pnnm* phases is defined by a positive Clapeyron slope, the structural transition and the elastic softening of δ-(Al,Fe)OOH might be occurring in the uppermost Earth's lower mantle (depth >660 km). The relevance of these phenomena in terms of seismic detectability will depend mostly on the volume fraction of δ-(Al,Fe)OOH in subducted lithologies.

Ultimately, and in a broader perspective, our results on δ-(Al,Fe)OOH also provide a better understanding of the relation between elasticity and hydrogen dynamics in other O-H···O-bearing materials, such as H_2O ices (e.g. Meier et al., 2018; Shi et al., 2021; Trybel et al., 2020) and phase D (Criniti et al., 2023; Thompson et al., 2022; Tsuchiya et al., 2005), where hydrogen bond symmetrization is predicted as well, although at higher pressures.

5. Acknowledgments

The authors thank Sumith Abeykoon for helping with the electron microprobe, and Raphael Njul for polishing the crystal platelets. Florian Trybel is acknowledged for fruitful discussions on hydrogen bond symmetrization. Michael Carpenter and another anonymous reviewer are acknowledged for their valuable suggestions. This research was supported by the International Research Training Group "Deep Earth Volatile Cycles" (GRK 2156/1) and the European Union's Horizon 2020 research and innovation Programme (ERC grant 864877). T. Ishii was supported by the Kakenhi Grant Number JP23K19067. An early draft of this manuscript was included in Satta (2021).

6. References

Angel, R. J. (2003). Automated profile analysis for single-crystal diffraction data. *Journal of Applied Crystallography*, *36*(2), Article 2. https://doi.org/10.1107/S0021889803001134

Angel, R. J., Alvaro, M., & Gonzalez-Platas, J. (2014). EosFit7c and a Fortran module (library) for equation of state calculations. *Zeitschrift Für Kristallographie - Crystalline Materials*, *229*(5). https://doi.org/10.1515/zkri-2013-1711

Angel, R. J., & Finger, L. W. (2011). SINGLE: A program to control single-crystal diffractometers. *Journal of Applied Crystallography*, *44*(1), 247–251. https://doi.org/10.1107/S0021889810042305

Arlt, T., & Angel, R. J. (2000). Displacive phase transitions in C-centred clinopyroxenes: Spodumene, LiScSi2O6 and ZnSiO3. *Physics and Chemistry of Minerals*, *27*(10), 719–731. https://doi.org/10.1007/s002690000116

Bercovici, D., & Karato, S. (2003). Whole-mantle convection and the transition-zone water filter. *Nature*, *425*(6953), 39–44.

Boehler, R., & De Hantsetters, K. (2004). New anvil designs in diamond-cells. *High Pressure Research*, *24*(3), 391–396. https://doi.org/10.1080/08957950412331323924

Boffa Ballaran, T., Angel, R. J., & Carpenter, M. A. (2000). High-pressure transformation behaviour of the cummingtonite-grunerite solid solution. *European Journal of Mineralogy*, *12*(6), 1195–1213. https://doi.org/10.1127/0935-1221/2000/0012-1195

Bolotina, N. B., Molchanov, V. N., Dyuzheva, T. I., Lityagina, L. M., & Bendeliani, N. A. (2008). Single-crystal structures of high-pressure phases FeOOH, FeOOD, and GaOOH. *Crystallography Reports*, *53*(6), 960–965. https://doi.org/10.1134/S1063774508060084

Buchen, J. (2018). *The Elastic Properties of Wadsleyite and Stishovite at High Pressures: Tracing Deep Earth Material Cycles*. University of Bayreuth. https://doi.org/10.15495/EPub_UBT_00004410

Buchen, J., Marquardt, H., Schulze, K., Speziale, S., Boffa Ballaran, T., Nishiyama, N., & Hanfland, M. (2018). Equation of State of Polycrystalline Stishovite Across the Tetragonal-Orthorhombic Phase Transition. *Journal of Geophysical Research: Solid Earth*, *123*(9), 7347–7360. https://doi.org/10.1029/2018JB015835

Buchen, J., Sturhahn, W., Ishii, T., & Jackson, J. M. (2021). Vibrational anisotropy of *δ*-(Al,Fe)OOH single crystals as probed by nuclear resonant inelastic X-ray scattering. *European Journal of Mineralogy*, *33*(4), 485–502. https://doi.org/10.5194/ejm-33-485-2021

Carpenter, M. A., Angel, R. J., & Finger, L. W. (1990). Calibration of Al/Si order variations in anorthite. *Contributions to Mineralogy and Petrology*, *104*(4), 471–480. https://doi.org/10.1007/BF01575624

Carpenter, M. A., Boffa Ballaran, T., & Atkinson, A. J. (1999). Microscopic strain, local structural heterogeneity and the energetics of silicate solid solutions. *Phase Transitions*, *69*(1), 95–109. https://doi.org/10.1080/01411599908208011

Carpenter, M. A., McKnight, R. E. A., Howard, C. J., Zhou, Q., Kennedy, B. J., & Knight, K. S. (2009). Characteristic length scale for strain fields around impurity cations in perovskites. *Physical Review B*, *80*(21), 214101. https://doi.org/10.1103/PhysRevB.80.214101

Carpenter, M. A., Meyer, H.-W., Sondergeld, P., Marion, S., & Knight, K. S. (2003). Spontaneous strain variations through the low temperature phase transitions of deuterated lawsonite. *American Mineralogist*, *88*(4), 534–546. https://doi.org/10.2138/am-2003-0407

Carpenter, M. A., Salje, E. K. H., & Graeme-Barber, A. (1998). Spontaneous strain as a determinant of thermodynamic properties for phase transitions in minerals. *European Journal of Mineralogy*, *10*(4), 621–691. https://doi.org/10.1127/ejm/10/4/0621

Carpenter, M. A., & Zhang, Z. (2011). Anelasticity maps for acoustic dissipation associated with phase transitions in minerals. *Geophysical Journal International*, *186*(1), 279–295. https://doi.org/10.1111/j.1365-246X.2011.05028.x

Cortona, P. (2017). Hydrogen bond symmetrization and elastic constants under pressure of δ-AlOOH. *Journal of Physics: Condensed Matter*, *29*(32), 325505. https://doi.org/10.1088/1361-648X/aa791f

Criniti, G., Ishii, T., Kurnosov, A., Glazyrin, K., Husband, R. J., & Ballaran, T. B. (2023). Structure and compressibility of Fe-bearing Al-phase D. *American Mineralogist*, *108*(9), 1764–1772. https://doi.org/10.2138/am-2022-8559

Dewaele, A., Loubeyre, P., & Mezouar, M. (2004). Equations of state of six metals above 94 GPa. *Physical Review B*, *70*(9), 094112. https://doi.org/10.1103/PhysRevB.70.094112

Every, A. G. (1980). General closed-form expressions for acoustic waves in elastically anisotropic solids. *Physical Review B*, *22*(4), 1746–1760. https://doi.org/10.1103/PhysRevB.22.1746

Gleason, A. E., Quiroga, C. E., Suzuki, A., Pentcheva, R., & Mao, W. L. (2013). Symmetrization driven spin transition in ε-FeOOH at high pressure. *Earth and Planetary Science Letters*, *379*, 49–55. https://doi.org/10.1016/j.epsl.2013.08.012

Haussühl, S. (2007). *Physical Properties of Crystals: An Introduction*. Wiley-VCH.

Hayward, S. A., & Salje, E. K. H. (1996). Displacive phase transition in anorthoclase; the “plateau effect” and the effect of T1-T2 ordering on the transition temperature. *American Mineralogist*, *81*(11–12), 1332–1336. https://doi.org/10.2138/am-1996-11-1204

Ikeda, O., Sakamaki, T., Ohashi, T., Goto, M., Higo, Y., & Suzuki, A. (2019). Sound velocity measurements of ε–FeOOH up to 24 GPa. *Journal of Mineralogical and Petrological Sciences*, *114*(3), 155–160. https://doi.org/10.2465/jmps.181115b

Insixiengmay, L., & Stixrude, L. (2023). Hydrogen bond symmetrization and high-spin to low-spin transition of ε-FeOOH at the pressure of Earth’s lower mantle. *American Mineralogist*, *108*(12), 2209–2218. https://doi.org/10.2138/am-2022-8839

Ishii, T., Criniti, G., Ohtani, E., Purevjav, N., Fei, H., Katsura, T., & Mao, H. (2022). Superhydrous aluminous silica phases as major water hosts in high-temperature lower mantle. *Proceedings of the National Academy of Sciences*, *119*(44), e2211243119. https://doi.org/10.1073/pnas.2211243119

Jacobsen, S. D. (2006). Effect of Water on the Equation of State of Nominally Anhydrous Minerals. *Reviews in Mineralogy and Geochemistry*, *62*(1), 321–342. https://doi.org/10.2138/rmg.2006.62.14

Kantor, I., Prakapenka, V., Kantor, A., Dera, P., Kurnosov, A., Sinogeikin, S., Dubrovinskaia, N., & Dubrovinsky, L. (2012). BX90: A new diamond anvil cell design for X-ray diffraction and optical measurements. *Review of Scientific Instruments*, *83*(12), 125102. https://doi.org/10.1063/1.4768541

King, H. E., & Finger, L. W. (1979). Diffracted beam crystal centering and its application to high-pressure crystallography. *Journal of Applied Crystallography*, *12*(4), 374–378. https://doi.org/10.1107/S0021889879012723

Klotz, S., Chervin, J.-C., Munsch, P., & Marchand, G. L. (2009). Hydrostatic limits of 11 pressure transmitting media. *Journal of Physics D: Applied Physics*, *42*(7), 075413. https://doi.org/10.1088/0022-3727/42/7/075413

Komatsu, K., Kuribayashi, T., Sano, A., Ohtani, E., & Kudoh, Y. (2006). Redetermination of the high-pressure modification of AlOOH from single-crystal synchrotron data. *Acta Crystallographica Section E: Structure Reports Online*, *62*(11), Article 11. https://doi.org/10.1107/S160053680603916X

Kuribayashi, T., Sano-Furukawa, A., & Nagase, T. (2014). Observation of pressure-induced phase transition of δ-AlOOH by using single-crystal synchrotron X-ray diffraction method. *Physics and Chemistry of Minerals*, *41*(4), 303–312. https://doi.org/10.1007/s00269-013-0649-6

Kurnosov, A., Kantor, I., Boffa-Ballaran, T., Lindhardt, S., Dubrovinsky, L., Kuznetsov, A., & Zehnder, B. H. (2008). A novel gas-loading system for mechanically closing of various types of diamond anvil cells. *Review of Scientific Instruments*, *79*(4), 045110. https://doi.org/10.1063/1.2902506

Lin, L., Morrone, J. A., & Car, R. (2011). Correlated Tunneling in Hydrogen Bonds. *Journal of Statistical Physics*, *145*(2), 365–384. https://doi.org/10.1007/s10955-011-0320-x

Lindsay, S. M., Anderson, M. W., & Sandercock, J. R. (1981). Construction and alignment of a high performance multipass vernier tandem Fabry–Perot interferometer. *Review of Scientific Instruments*, *52*(10), 1478–1486. https://doi.org/10.1063/1.1136479

Luo, C., Umemoto, K., & Wentzcovitch, R. M. (2022). Ab initio investigation of H-bond disordering in \ensuremath{\delta}-AlOOH. *Physical Review Research*, *4*(2), 023223. https://doi.org/10.1103/PhysRevResearch.4.023223

Ma, T., Hou, S., Yu, F., Xie, C., Zhang, S., Wang, J., Du, J., Zhan, J., Cheng, X., Wang, S., & Zhao, X. (2017). Electro-elastic characterization of Ca3TaGa3Si2O14 crystals for lateral-field-excitation acoustic wave sensing applications. *Journal of Alloys and Compounds*, *728*, 518–524. https://doi.org/10.1016/j.jallcom.2017.08.284

Marquardt, H., Gleason, A., Marquardt, K., Speziale, S., Miyagi, L., Neusser, G., Wenk, H.-R., & Jeanloz, R. (2011). Elastic properties of MgO nanocrystals and grain boundaries at high pressures by Brillouin scattering. *Physical Review B*, *84*(6), 064131. https://doi.org/10.1103/PhysRevB.84.064131

Mashino, I., Murakami, M., & Ohtani, E. (2016). Sound velocities of δ-AlOOH up to core-mantle boundary pressures with implications for the seismic anomalies in the deep mantle. *Journal of Geophysical Research: Solid Earth*, *121*(2), 595–609. https://doi.org/10.1002/2015JB012477

McConnell, J. D. C., McCammon, C. A., Angel, R. J., & Seifert, F. (2000). The nature of the incommensurate structure in åkermanite, Ca2MgSi2O7, and the character of its transformation from the normal structure. *Zeitschrift Für Kristallographie - Crystalline Materials*, *215*(11), 669–677. https://doi.org/10.1524/zkri.2000.215.11.669

Meier, T., Aslandukova, A., Trybel, F., Laniel, D., Ishii, T., Khandarkhaeva, S., Dubrovinskaia, N., & Dubrovinsky, L. (2021). In situ high-pressure nuclear magnetic resonance crystallography in one and two dimensions. *Matter and Radiation at Extremes*, *6*(6), 068402. https://doi.org/10.1063/5.0065879

Meier, T., Petitgirard, S., Khandarkhaeva, S., & Dubrovinsky, L. (2018). Observation of nuclear quantum effects and hydrogen bond symmetrisation in high pressure ice. *Nature Communications*, *9*(1), Article 1. https://doi.org/10.1038/s41467-018-05164-x

Meier, T., Trybel, F., Khandarkhaeva, S., Laniel, D., Ishii, T., Aslandukova, A., Dubrovinskaia, N., & Dubrovinsky, L. (2022). Structural independence of hydrogen-bond symmetrisation dynamics at extreme pressure conditions. *Nature Communications*, *13*(1), 3042. https://doi.org/10.1038/s41467-022-30662-4

Méndez, A. S. J., Trybel, F., Husband, R. J., Steinle-Neumann, G., Liermann, H.-P., & Marquardt, H. (2021). Bulk modulus of H2O across the ice VII--ice X transition measured by time-resolved x-ray diffraction in dynamic diamond anvil cell experiments. *Physical Review B*, *103*(6), 064104. https://doi.org/10.1103/PhysRevB.103.064104

Nishi, M., Tsuchiya, J., Kuwayama, Y., Arimoto, T., Tange, Y., Higo, Y., Hatakeyama, T., & Irifune, T. (2019). Solid Solution and Compression Behavior of Hydroxides in the Lower Mantle. *Journal of Geophysical Research: Solid Earth*, *124*(10), 10231–10239. https://doi.org/10.1029/2019JB018146

Nye, J. F. (1985). *Physical Properties of Crystals: Their Representation by Tensors and Matrices*. Oxford University Press.

Ohira, I., Jackson, J. M., Solomatova, N. V., Sturhahn, W., Finkelstein, G. J., Kamada, S., Kawazoe, T., Maeda, F., Hirao, N., Nakano, S., Toellner, T. S., Suzuki, A., & Ohtani, E. (2019). Compressional behavior and spin state of δ-(Al,Fe)OOH at high pressures. *American Mineralogist*, *104*(9), 1273–1284. https://doi.org/10.2138/am-2019-6913

Ohira, I., Ohtani, E., Sakai, T., Miyahara, M., Hirao, N., Ohishi, Y., & Nishijima, M. (2014). Stability of a hydrous δ-phase, AlOOH–MgSiO2(OH)2, and a mechanism for water transport into the base of lower mantle. *Earth and Planetary Science Letters*, *401*, 12–17. https://doi.org/10.1016/j.epsl.2014.05.059

Ohno, I. (1990). Rectangular parallellepiped resonance method for piezoelectric crystals and elastic constants of alpha-quartz. *Physics and Chemistry of Minerals*, *17*(5), 371–378. https://doi.org/10.1007/BF00212204

Ohtani, E. (2015). Hydrous minerals and the storage of water in the deep mantle. *Chemical Geology*, *418*, 6–15. https://doi.org/10.1016/j.chemgeo.2015.05.005

Ohtani, E. (2020). The role of water in Earth's mantle. *National Science Review*, *7*(1), 224–232. https://doi.org/10.1093/nsr/nwz071

Ohtani, E., Litasov, K., Hosoya, T., Kubo, T., & Kondo, T. (2004). Water transport into the deep mantle and formation of a hydrous transition zone. *Physics of the Earth and Planetary Interiors*, *143–144*, 255–269. https://doi.org/10.1016/j.pepi.2003.09.015

Panero, W. R., & Stixrude, L. P. (2004). Hydrogen incorporation in stishovite at high pressure and symmetric hydrogen bonding in δ-AlOOH. *Earth and Planetary Science Letters*, *221*(1), 421–431. https://doi.org/10.1016/S0012-821X(04)00100-1

Pernet, M., Joubert, J. C., & Berthet-Colominas, C. (1975). Etude par diffraction neutronique de la forme haute pression de FeOOH. *Solid State Communications*, *17*(12), 1505–1510. https://doi.org/10.1016/0038-1098(75)90983-7

Pillai, S. B., Jha, P. K., Padmalal, A., Maurya, D. M., & Chamyal, L. S. (2018). First principles study of hydrogen bond symmetrization in δ-AlOOH. *Journal of Applied Physics*, *123*(11), 115901. https://doi.org/10.1063/1.5019586

Sandercock, J. R. (1982). *Trends in brillouin scattering: Studies of opaque materials, supported films, and central modes* (pp. 173–206). Springer, Berlin, Heidelberg. https://doi.org/10.1007/3540115137_6

Sano-Furukawa, A., Hattori, T., Komatsu, K., Kagi, H., Nagai, T., Molaison, J. J., dos Santos, A. M., & Tulk, C. A. (2018). Direct observation of symmetrization of hydrogen bond in δ-AlOOH under mantle conditions using neutron diffraction. *Scientific Reports*, *8*(1), Article 1. https://doi.org/10.1038/s41598-018-33598-2

Sano-Furukawa, A., Kagi, H., Nagai, T., Nakano, S., Fukura, S., Ushijima, D., Iizuka, R., Ohtani, E., & Yagi, T. (2009). Change in compressibility of δ-AlOOH and δ-AlOOD at high pressure: A study of isotope effect and hydrogen-bond symmetrization. *American Mineralogist*, *94*(8–9), 1255–1261. https://doi.org/10.2138/am.2009.3109

Satta, N. (2021). *High Pressure Minerals in the Earth and Moon: Understanding the Lunar Impact History and Earth's Deep Water Cycle* [Doctoral thesis]. https://doi.org/10.15495/EPub_UBT_00005517

Satta, N., Criniti, G., Kurnosov, A., Boffa Ballaran, T., Ishii, T., & Marquardt, H. (2021). High-Pressure Elasticity of δ-(Al,Fe)OOH Single Crystals and Seismic Detectability of Hydrous MORB in the Shallow Lower Mantle. *Geophysical Research Letters*, *48*(23), e2021GL094185. https://doi.org/10.1029/2021GL094185

Schulze, K., Buchen, J., Marquardt, K., & Marquardt, H. (2017). Multi-sample loading technique for comparative physical property measurements in the diamond-anvil cell. *High Pressure Research*, *37*(2), 159–169. https://doi.org/10.1080/08957959.2017.1299719

Shi, W., Sun, N., Li, X., Mao, Z., Liu, J., & Prakapenka, V. B. (2021). Single-Crystal Elasticity of High-Pressure Ice up to 98 GPa by Brillouin Scattering. *Geophysical Research Letters*, *48*(8), e2021GL092514. https://doi.org/10.1029/2021GL092514

Simonova, D., Bykova, E., Bykov, M., Kawazoe, T., Simonov, A., Dubrovinskaia, N., & Dubrovinsky, L. (2020). Structural Study of δ-AlOOH Up to 29 GPa. *Minerals*, *10*(12), Article 12. https://doi.org/10.3390/min10121055

Speziale, S., Marquardt, H., & Duffy, T. S. (2014). Brillouin Scattering and its Application in Geosciences. *Reviews in Mineralogy and Geochemistry*, *78*(1), 543–603. https://doi.org/10.2138/rmg.2014.78.14

Stixrude, L., & Lithgow-Bertelloni, C. (2005). Thermodynamics of mantle minerals—I. Physical properties. *Geophysical Journal International*, *162*(2), 610–632. https://doi.org/10.1111/j.1365-246X.2005.02642.x

Strozewski, B., Buchen, J., Sturhahn, W., Ishii, T., Ohira, I., Chariton, S., Lavina, B., Zhao, J., Toellner, T. S., & Jackson, J. M. (2023). Equation of State and Spin Crossover of (Al, Fe)-Phase H. *Journal of Geophysical Research: Solid Earth*, *128*(4), e2022JB026291. https://doi.org/10.1029/2022JB026291

Su, X., Zhao, C., Lv, C., Zhuang, Y., Salke, N., Xu, L., Tang, H., Gou, H., Yu, X., Sun, Q., & Liu, J. (2020). The effect of iron on the sound velocities of δ-AlOOH up to 135 GPa. *Geoscience Frontiers*, *12*(2), 937–946. https://doi.org/10.1016/j.gsf.2020.08.012

Sugimura, E., Iitaka, T., Hirose, K., Kawamura, K., Sata, N., & Ohishi, Y. (2008). Compression of H20 ice to 126 GPa and implications for hydrogen-bond symmetrization: Synchrotron x-ray diffraction measurements and density-functional calculations. *Physical Review B*, *77*(21), 214103. https://doi.org/10.1103/PhysRevB.77.214103

Suzuki, A. (2010). High-pressure X-ray diffraction study of ε-FeOOH. *Physics and Chemistry of Minerals*, *37*(3), 153–157. https://doi.org/10.1007/s00269-009-0319-x

Suzuki, A., Ohtani, E., & Kamada, T. (2000). A new hydrous phase δ-AlOOH synthesized at 21 GPa and 1000 °C. *Physics and Chemistry of Minerals*, *27*(10), 689–693. https://doi.org/10.1007/s002690000120

Thompson, E. C., Campbell, A. J., & Tsuchiya, J. (2017). Elasticity of ε-FeOOH: Seismic implications for Earth's lower mantle. *Journal of Geophysical Research: Solid Earth*, *122*(7), 5038–5047. https://doi.org/10.1002/2017JB014168

Thompson, E. C., Campbell, A. J., & Tsuchiya, J. (2022). Calculated Elasticity of Al-Bearing Phase D. *Minerals*, *12*(8), Article 8. https://doi.org/10.3390/min12080922

Thompson, E. C., Davis, A. H., Brauser, N. M., Liu, Z., Prakapenka, V. B., & Campbell, A. J. (2020). Phase transitions in ε-FeOOH at high pressure and ambient temperature. *American Mineralogist*, *105*(12), 1769–1777. https://doi.org/10.2138/am-2020-7468

Trots, D. M., Kurnosov, A., Boffa Ballaran, T., Tkachev, S., Zhuravlev, K., Prakapenka, V., Berkowski, M., & Frost, D. J. (2013). The Sm:YAG primary fluorescence pressure scale. *Journal of Geophysical Research: Solid Earth*, *118*(11), 5805–5813. https://doi.org/10.1002/2013JB010519

Trots, D. M., Kurnosov, A., Vasylechko, L., Berkowski, M., Boffa Ballaran, T., & Frost, D. J. (2011). Elasticity and equation of state of Li2B4O7. *Physics and Chemistry of Minerals*, *38*(7), 561. https://doi.org/10.1007/s00269-011-0428-1

Trybel, F., Cosacchi, M., Meier, T., Axt, V. M., & Steinle-Neumann, G. (2020). Proton dynamics in high-pressure ice-VII from density functional theory. *Physical Review B*, *102*(18), 184310. https://doi.org/10.1103/PhysRevB.102.184310

Trybel, F., Meier, T., Wang, B., & Steinle-Neumann, G. (2021). Absence of proton tunneling during the hydrogen-bond symmetrization in δ-AlOOH. *Physical Review B*, *104*(10), 104311. https://doi.org/10.1103/PhysRevB.104.104311

Tsuchiya, J., & Tsuchiya, T. (2009). Elastic properties of δ-AlOOH under pressure: First principles investigation. *Physics of the Earth and Planetary Interiors*, *174*(1–4), 122–127. https://doi.org/10.1016/j.pepi.2009.01.008

Tsuchiya, J., Tsuchiya, T., & Tsuneyuki, S. (2005). First-principles study of hydrogen bond symmetrization of phase D under high pressure. *American Mineralogist*, *90*(1), 44–49. https://doi.org/10.2138/am.2005.1628

Tsuchiya, J., Tsuchiya, T., Tsuneyuki, S., & Yamanaka, T. (2002). First principles calculation of a high-pressure hydrous phase, δ-AlOOH. *Geophysical Research Letters*, *29*(19), 15-1-15–4. https://doi.org/10.1029/2002GL015417

Tsuchiya, T., Tsuchiya, J., Dekura, H., & Ritterbex, S. (2020). Ab Initio Study on the Lower Mantle Minerals. *Annual Review of Earth and Planetary Sciences*, *48*(1), 99–119. https://doi.org/10.1146/annurev-earth-071719-055139

Wang, B., Buchen, J., Méndez, A. S. J., Kurnosov, A., Criniti, G., Liermann, H.-P., & Marquardt, H. (2023). Strong Effect of Stress on the Seismic Signature of the Post-Stishovite Phase Transition in the Earth's Lower Mantle. *Geophysical Research Letters*, *50*(10), e2023GL102740. https://doi.org/10.1029/2023GL102740

Wang, B., Tan, D., Xiao, W., Ding, X., Li, L., & Song, M. (2022). Raman scattering and Cr3+ luminescence study on the structural behavior of δ-AlOOH at high pressures. *American Mineralogist*, *107*(10), 1858–1867. https://doi.org/10.2138/am-2022-8005

Wang, B., Zhang, Y., Fu, S., Yan, W., Takahashi, E., Li, L., Lin, J.-F., & Song, M. (2022). Single-crystal elasticity of phase Egg AlSiO3OH and δ-AlOOH by Brillouin spectroscopy. *American Mineralogist*, *107*(1), 147–152. https://doi.org/10.2138/am-2022-8056

Whitfield, C. H., Brody, E. M., & Bassett, W. A. (1976). Elastic moduli of NaCl by Brillouin scattering at high pressure in a diamond anvil cell. *Review of Scientific Instruments*, *47*(8), 942–947. https://doi.org/10.1063/1.1134778

Xu, W., Greenberg, E., Rozenberg, G. Kh., Pasternak, M. P., Bykova, E., Boffa-Ballaran, T., Dubrovinsky, L., Prakapenka, V., Hanfland, M., Vekilova, O. Yu., Simak, S. I., & Abrikosov, I. A. (2013). Pressure-Induced Hydrogen Bond Symmetrization in Iron Oxyhydroxide. *Physical Review Letters*, *111*(17), 175501. https://doi.org/10.1103/PhysRevLett.111.175501

Zhang, Y., Fu, S., Wang, B., & Lin, J.-F. (2021). Elasticity of a Pseudoproper Ferroelastic Transition from Stishovite to Post-Stishovite at High Pressure. *Physical Review Letters*, *126*(2), 025701. https://doi.org/10.1103/PhysRevLett.126.025701

7. List of Figure Captions

Figure 1. Intensity (I) of the $0\bar{3}0$ reflection normalized with respect to the intensity of the $1\bar{3}0$ reflection collected at the same pressure, and as function of pressure (P). Note that $0\bar{3}0$ is present in the $P2_1nm$ space group and is a systematic absence in the $Pnnm$ space group. Solid line results from a fit to the observed intensity ratios using Equation 3. The inset shows rocking curves (omega scans) of the $0\bar{3}0$ diffraction peak collected at different pressures. Color scale links each curve to its respective collection pressure (values in GPa).

Figure 2. a) Unit-cell volume (V/V_0) and b) axial (l/l_0) compression for δ-$(Al_{0.97},Fe_{0.03})OOH$ as function of pressure (P). Note that the unit-cell volumes and unit-cell axes were normalized with respect their values observed at room pressure. In our data, open symbols represent data points collected in the proximity of the $P2_1nm$-$Pnnm$ transition, and at pressures of 7.06(5), 7.44(2) and 7.59(3) GPa. These data points were not included in the refinement of BM3 parameters. Solid and dashed lines represent a BM3 fit to our observations (excluding those at $P_{\mathrm{ruby}} \geq 7.06(5)$ GPa) and extrapolations to higher pressures, respectively. Inset in (a) shows differences between pressures determined using the ruby fluorescence P_{ruby} (Table S1 in Supporting Information), and those calculated using the BM3 parameters (P_{calc}, Table S1 in Supporting Information) as a function of P_{ruby}. Error bars are the sum of the uncertainty on P_{ruby}, calculated as the semi-difference between P_{ruby} before and after the XRD measurements, and P_{calc}, obtained by propagating the uncertainties on the BM3 fit parameters using the full covariance matrix.

Figure 3. Results from high-pressure Brillouin spectroscopy experiments on δ-$(Al_{0.97},Fe_{0.03})OOH$. a) Representative Brillouin spectrum, collected on H4765x1 at rotation angle (χ) = -30° and P_{ruby}=3.85(7) GPa. Spectral contributions are assigned to the sample compressional

(v_P), fast shear (v_{S1}) and slow shear (v_{S2}) wave velocities, compressional wave velocity of the pressure transmitting medium (Ne) and its backscattered signal (BS), diamond-anvil shear wave velocity (D) and elastic scattering (R). b) Observed (solid symbols) and calculated (solid lines) acoustic wave velocities of both platelets as a function of the rotation angle (χ) at P_{ruby}=6.46(2) GPa.

Figure 4. Single-crystal elastic stiffness coefficients (c_{ij}) of δ-($Al_{0.97}$,$Fe_{0.03}$)OOH as function of pressure (*P*). a) c_{11}, c_{22} and c_{33}; b) c_{44}, c_{55} and c_{66}; c) c_{12}, c_{13} and c_{23}. Solid and open circles are c_{ij} constrained in this study for the $P2_1nm$ phase of δ-($Al_{0.97}$,$Fe_{0.03}$)OOH, while solid squares are c_{ij} of *Pnnm* phase. Solid line are least square fits to our $P2_1nm$ phase data of third-order finite strain equations (Stixrude & Lithgow-Bertelloni, 2005). Note that c_{ij} constrained at pressures close to the $P2_1nm$-*Pnnm* transition [open circles, $P_{\mathrm{ruby}} \geq 7.06(5)$ GPa] were not considered in the fit. Dashed lines are extrapolation of the $P2_1nm$ phase data fit. Dash-dot lines show the high-pressure behaviour of c_{ij} belonging to the *Pnnm* phase of δ-($Al_{0.97}$,$Fe_{0.03}$)OOH as reported by Satta et al. (2021). The short-dotted lines show the Landau-based model predictions for c_{ij} in the $P2_1nm$ phase field. Solid vertical line shows transition pressure [$P_c = 7.7(2)$ GPa] as determined from fit of Q^2 to experimental observations, with the grey region indicating the uncertainty on the transition pressure. Literature references for δ-AlOOH are: 1) Wang et al. (2022); 2) Cortona (2017); 3) Tsuchiya & Tsuchiya (2009); 4) Pillai et al. (2018).

Figure 5. Aggregate properties of δ-($Al_{0.97}$,$Fe_{0.03}$)OOH as function of pressure (*P*): a) aggregate elastic modulus (*M*); b) aggregate velocity (*v*). For this study, solid and open circles are values calculated for the $P2_1nm$ phase of δ-($Al_{0.97}$,$Fe_{0.03}$)OOH, while solid squares are those of the *Pnnm* phase. Solid line results from least square fits to our $P2_1nm$ phase data of third-order finite strain equations (Stixrude & Lithgow-Bertelloni, 2005). Note that the values constrained at

pressures close to the $P2_1nm \rightarrow Pnnm$ transition (open circles, $P_{\mathrm{ruby}} \geq 7.06(5)$ GPa) were not considered in the fit. Dashed lines are extrapolation of the $P2_1nm$ phase data fit. Dashed-point lines show the high-pressure behaviour of c_{ij} of the *Pnnm* phase of δ-($Al_{0.97}$,$Fe_{0.03}$)OOH from Satta et al. (2021). The short-dotted lines show the Landau-based model predictions for c_{ij} in the $P2_1nm$ phase field. Solid vertical line shows transition pressure [$P_c = 7.7(2)$ GPa] as determined from fit of Q^2 to experimental observations, with the grey region indicating the uncertainty on the transition pressure. In Figure a), literature references for δ-AlOOH are: 1) Wang et al. (2022); 2) Cortona (2017); 3) Tsuchiya & Tsuchiya (2009); 4) Pillai et al. (2018). In Figure b), literature references are: 1) Wang et al. (2022); δ-AlOOH; 2) Mashino et al. (2016), δ-AlOOH; 3) Su et al. (2020), δ-($Al_{0.95}$,$Fe_{0.05}$)OOH

8. Tables

Table 1. Elastic stiffness coefficients (c_{ij}), aggregate elastic moduli (M_0) and their pressure derivatives (M'_0) of the $P2_1nm$ phase of δ–($Al_{0.97}$,$Fe_{0.03}$)OOH. Results are obtained from the fit of third-order Eulerian strain equations (Equation 4) to c_{ij} constrained at $P_{ruby} \leq 6.46(5)$ GPa.

ij	c_{ij0} (GPa)	c'_{ij0}		M_0 (GPa)	M'_0
11	370(2.6)	9.9(5)	Voigt Bound		
22	300(4)	5(1)	K_{S0}^{V}	165(2)	3.6(5)
33	413(4)	5.1(9)	G_0^{V}	143(1)	2.7(2)
44	127.6(13)	2.6(2)	Reuss Bound		
55	127.4(8)	1.6(2)	K_{S0}^{R}	160(2.2)	3.6(5)
66	169(2)	4.4(5)	G_0^{R}	141(1)	2.7(2)
12	48(4)	1.7(10)	Voigt-Reuss-Hill average		
13	98(3)	2.4(7)	K_{S0}^{H}	163(2)	3.6(5)
23	59(4)	1.6(9)	G_0^{H}	142(1)	2.7(2)

9. Figures

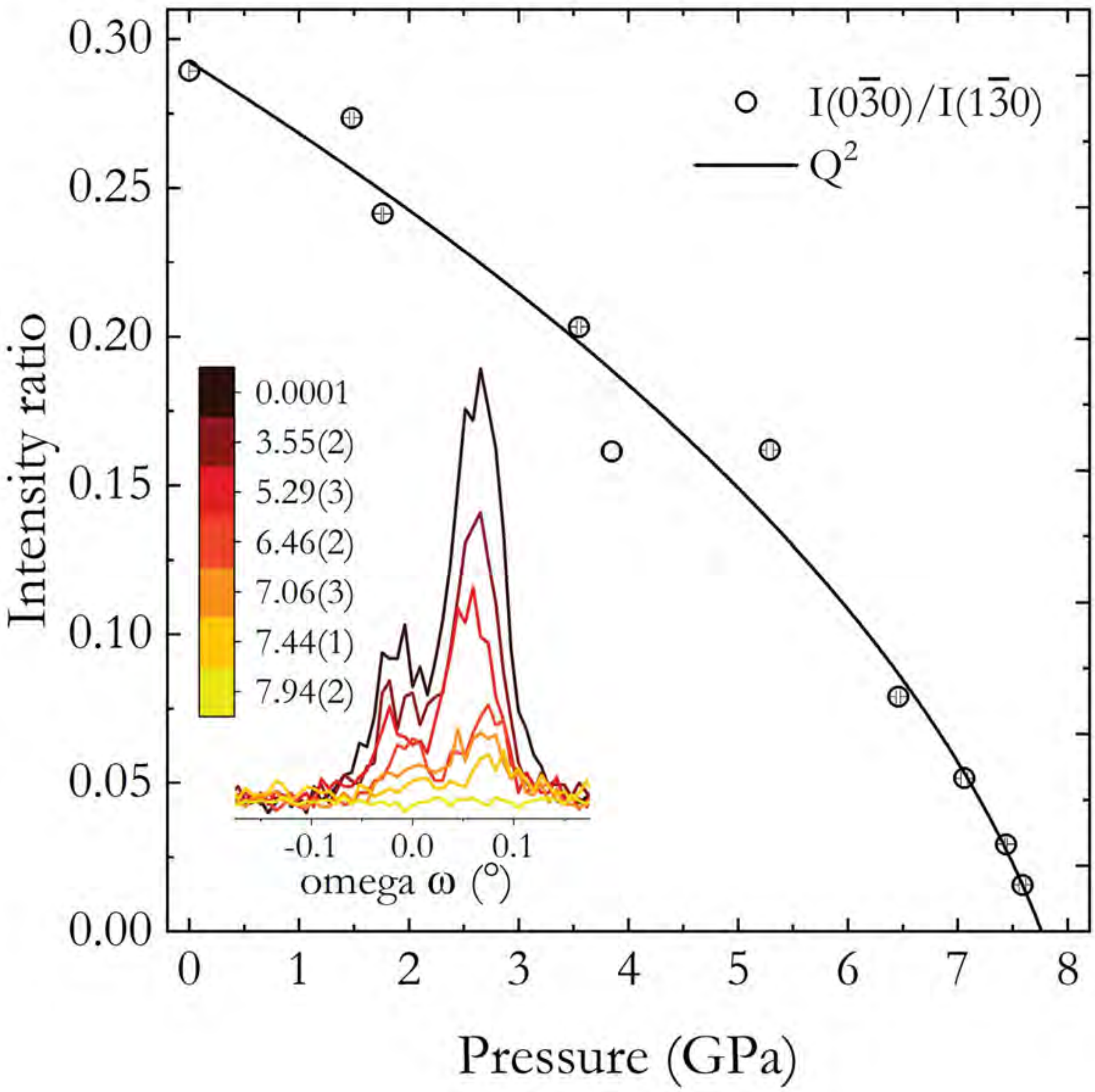

Figure 1.

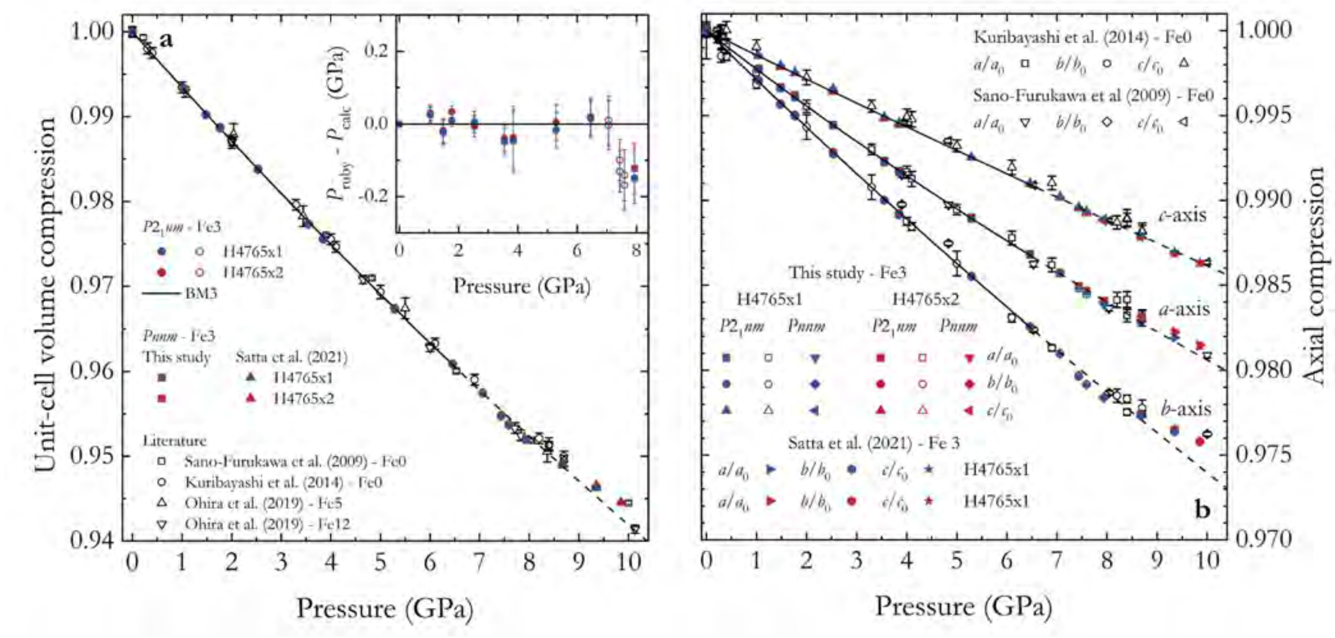
a
Unit-cell volume compression
Pressure (GPa)
$P_{ruby} - P_{calc}$ (GPa)
Pressure (GPa)
$P2_1nm$ - Fe3
H4765x1
H4765x2
BM3
$Pnnm$ - Fe3
This study
Satta et al. (2021)
H4765x1
H4765x2
Literature
Sano-Furukawa et al. (2009) - Fe0
Kuribayashi et al. (2014) - Fe0
Ohira et al. (2019) - Fe5
Ohira et al. (2019) - Fe12
b
Axial compression
Pressure (GPa)
Kuribayashi et al. (2014) - Fe0
a/a_0 b/b_0 c/c_0
Sano-Furukawa et al (2009) - Fe0
a/a_0 b/b_0 c/c_0
This study - Fe3
H4765x1
H4765x2
$P2_1nm$ $Pnnm$ $P2_1nm$ $Pnnm$
a/a_0
b/b_0
c/c_0
Satta et al. (2021) - Fe 3
a/a_0 b/b_0 c/c_0 H4765x1
a/a_0 b/b_0 c/c_0 H4765x1
c-axis
a-axis
b-axis

Figure 2.

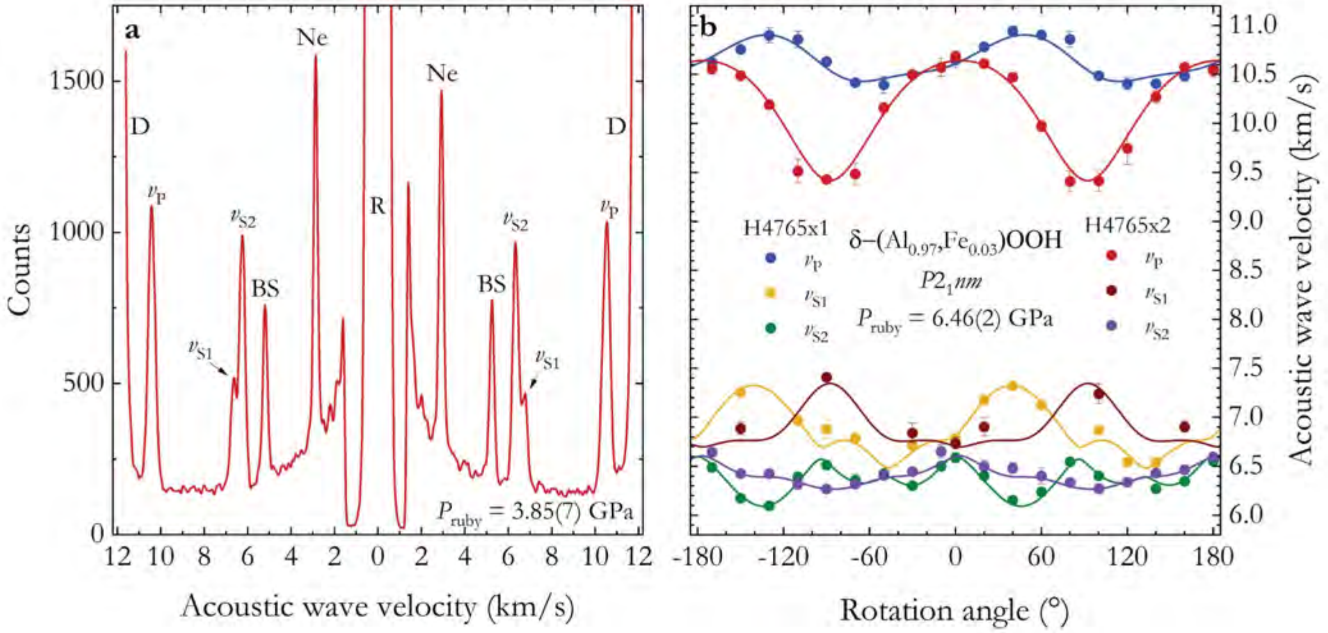
a
Counts
1500
1000
500
0
D
v_P
v_{S2}
v_{S1}
BS
Ne
R
Ne
BS
v_{S2}
v_{S1}
v_P
D
P_{ruby} = 3.85(7) GPa
12 10 8 6 4 2 0 2 4 6 8 10 12
Acoustic wave velocity (km/s)
b
H4765x1
v_P
v_{S1}
v_{S2}
δ–($Al_{0.97}$,$Fe_{0.03}$)OOH
$P2_1nm$
P_{ruby} = 6.46(2) GPa
H4765x2
v_P
v_{S1}
v_{S2}
11.0
10.5
10.0
9.5
9.0
8.5
8.0
7.5
7.0
6.5
6.0
Acoustic wave velocity (km/s)
-180 -120 -60 0 60 120 180
Rotation angle (°)

Figure 3.

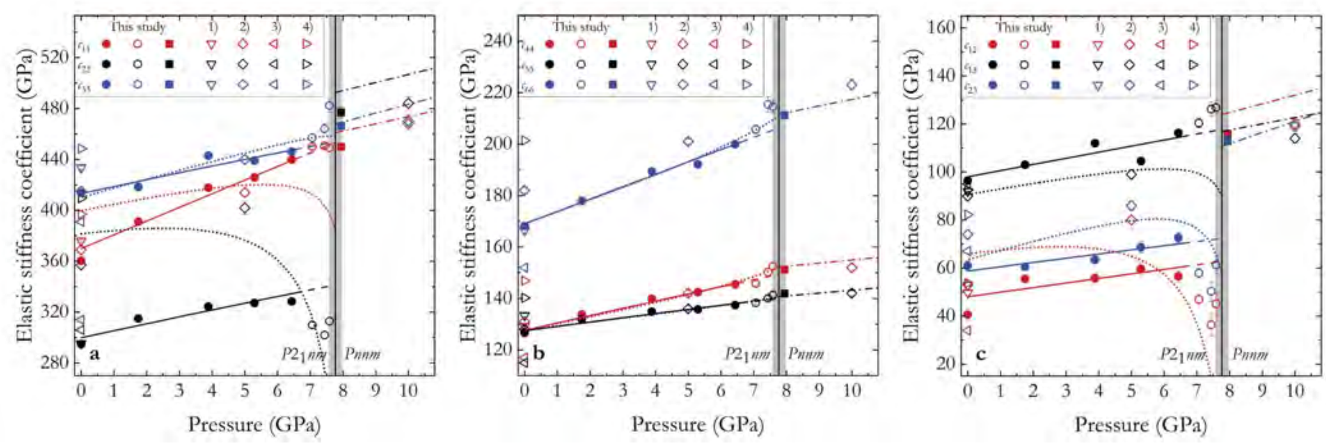
This study
1)
2)
3)
4)
c_{11}
c_{22}
c_{33}
c_{44}
c_{55}
c_{66}
c_{12}
c_{13}
c_{23}
Elastic stiffness coefficient (GPa)
Pressure (GPa)
a
b
c
$P2_1nm$
$Pnnm$
280
320
360
400
440
480
520
120
140
160
180
200
220
240
20
40
60
80
100
120
140
160
0
1
2
3
4
5
6
7
8
9
10

Figure 4.

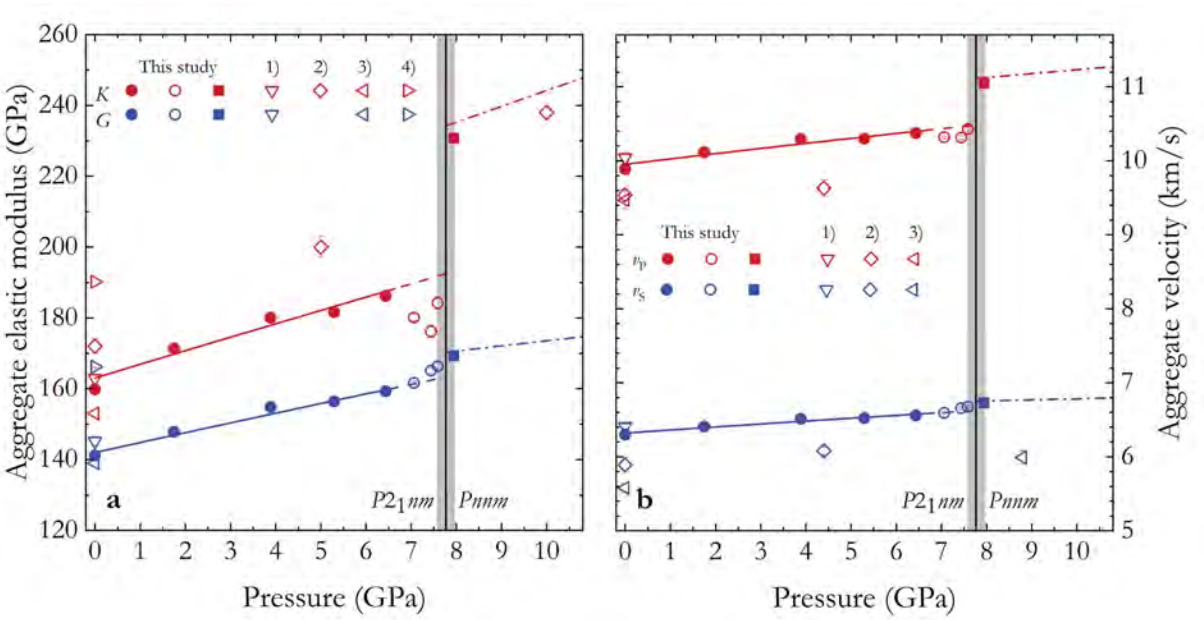
This study
1)
2)
3)
4)
K ● ○ ■ ▽ ◇ ◁ ▷
G ● ○ ■ ▽ ◁ ▷
Aggregate elastic modulus (GPa)
260
240
220
200
180
160
140
120
a
P2₁nm
Pnnm
0 1 2 3 4 5 6 7 8 9 10
Pressure (GPa)
This study
1)
2)
3)
v_P ● ○ ■ ▽ ◇ ◁
v_S ● ○ ■ ▽ ◇ ◁
b
P2₁nm
Pnnm
Aggregate velocity (km/s)
11
10
9
8
7
6
5
0 1 2 3 4 5 6 7 8 9 10
Pressure (GPa)

Figure 5